High resolution combined molecular and structural optical imaging of colorectal cancer in a xenograft mouse model

Feroldi, Fabio; Verlaan, Mariska; Knaus, Helene; Davidoiu, Valentina; Vugts, Danielle J.; Van Dongen, Guus A.M.S.; Molthoff, Carla F.M.; De Boer, Johannes F.

published in
Biomedical Optics Express
2018

DOI (link to publisher)
10.1364/BOE.9.006186

Research Article | Vol. 9, No. 12 | 1 Dec 2018 | BIOMEDICAL OPTICS EXPRESS 6186
Biomedical Optics EXPRESS

High resolution combined molecular and structural optical imaging of colorectal cancer in a xenograft mouse model

FABIO FEROLDI,[1,*] MARISKA VERLAAN,[2] HELENE KNAUS,[1] VALENTINA DAVIDOIU,[1] DANIELLE J. VUGTS,[2] GUUS A. M. S. VAN DONGEN,[2] CARLA F. M. MOLTHOFF,[2] AND JOHANNES F. DE BOER[1]

[1]*Department of Physics and Astronomy, LaserLaB Amsterdam, VU University Amsterdam, de Boelelaan 1081, 1081HV, Amsterdam, The Netherlands*
[2]*Amsterdam UMC, Vrije Universiteit Amsterdam, Department of Radiology & Nuclear Medicine, De Boelelaan 1117, 1081 HV Amsterdam, The Netherlands*
**fabio.feroldi@vu.nl*

Abstract: With the emergence of immunotherapies for cancer treatment, there is a rising clinical need to visualize the tumor microenvironment (TME) non-invasively in detail, which could be crucial to predict the efficacy of therapy. Nuclear imaging techniques enable whole-body imaging but lack the required spatial resolution. Conversely, near-infrared immunofluorescence (immuno-NIRF) is able to reveal tumor cells and/or other cell subsets in the TME by targeting the expression of a specific membrane receptor with fluorescently labeled monoclonal antibodies (mAb). Optical coherence tomography (OCT) provides three-dimensional morphological imaging of tissues without exogenous contrast agents. The combination of the two allows molecular and structural contrast at a resolution of ~15 µm, allowing for the specific location of a cell-type target with immuno-NIRF as well as revealing the three-dimensional architectural context with OCT. For the first time, combined immuno-NIRF and OCT of a tumor is demonstrated *in situ* in a xenograft mouse model of human colorectal cancer, targeted by a clinically-safe fluorescent mAb, revealing unprecedented details of the TME. A handheld scanner for *ex vivo* examination and an endoscope designed for imaging bronchioles *in vivo* are presented. This technique promises to complement nuclear imaging for diagnosing cancer invasiveness, precisely determining tumor margins, and studying the biodistribution of newly developed antibodies in high detail.

1. Introduction

Over the past two decades, immunotherapy has attracted interest as a potentially revolutionary technique in cancer treatment. There are several immunotherapy strategies, for example, using monoclonal antibodies (mAbs) to stimulate the body's immune response to attack the cancerous cells [1], inhibiting tumor growth by blocking receptors or growth factors with mAbs [2], or even specifically deliver cytotoxic drugs to cancer cells with antibody-drug conjugates [3,4]. To predict treatment outcome and/or monitor treatment success, imaging techniques showing the biodistribution of these mAbs *in vivo* are needed. In particular, assessing the degree of heterogeneity of the tumor microenvironment (TME) and the interaction between immune cells and tumor cells have been suggested as a prognostic marker [5]. Non-invasively diagnosing the infiltration of a tumor into the mucosa and submucosa could be achieved by molecular imaging using mAbs, therefore avoiding taking biopsies. Moreover, identification of the tumor margin and real-time tumor specific imaging would help in image-guided surgery.

One approach is radioactively labeling the antibody and following its distribution with positron emission tomography (PET) or single-photon emission computed tomography

#346860 https://doi.org/10.1364/BOE.9.006186
Journal © 2018 Received 28 Sep 2018; revised 1 Nov 2018; accepted 6 Nov 2018; published 13 Nov 2018

Biomedical Optics EXPRESS

(SPECT). The combination with morphological imaging provided by computed tomography (CT) or magnetic resonance imaging (MRI) is particularly powerful, because it allows the identification of the anatomical location targeted by a mAb and provides the architectural context at a whole body level. The limited spatial resolution of around 5 mm of PET and SPECT, however, does not permit studying the TME in sufficient detail and to accurately define tumor margins, tumor invasiveness, and the cellular composition of tumors. Moreover, PET and SPECT have a scan time of about 1 hour, prohibiting real time imaging for image-aided surgery. Finally, only one marker at a time can be tracked with nuclear imaging. These limitations can be overcome with optical techniques, such as fluorescence imaging, which typically have a resolution in the order of microns, allowing imaging at the (sub-)cellular level, have a typical scan time of a few seconds to minutes and allow imaging multiple mAbs by using spectrally separated fluorophores. Although the penetration depth of light in tissue is limited, most tumors originate at the epithelial layers of organs, and are therefore in the large majority of cases accessible through endoscopic imaging. Labeling mAbs with fluorescent molecules for targeted imaging has been demonstrated in the early 90's [6–8] and has gained new interest for *in vivo* imaging with the development of conjugation-suitable near infrared fluorophores [9–12].

Tumors in the lumen walls of organs such as colon, esophagus, and lungs, are accessible by purposely-designed endoscopes. Technical advancements facilitated the progress towards increasingly compact endoscopic optical coherence tomography (OCT)-fluorescence systems [13–22], in particular the development of highly efficient double-clad fiber couplers [23,24]. To date, only two studies have combined OCT and immuno-fluorescence in an endoscopic platform, but in both cases the experiments were performed on excised tissue only. Liang *et al.* [25] stained aorta tissue sections from rabbits with atherosclerosis with Annexin-Cy5.5 (excitation peak 675 nm), which allowed identification of necrotic and inflamed regions. Scolaro *et al.* [26] imaged excised mouse liver incubated with an EpCAM antibody conjugated to Alexa Fluor 488 (490 nm excitation peak), allowing identification of epithelial cells specifically. Several drawbacks in using visible-region wavelengths were identified, including limited penetration depth, conspicuous tissue autofluorescence [27], and reduced permitted illumination fluence. Most importantly, none of these dyes is in the process of being translated into clinical use [28]. Compared to fluorophores in the visible range, excitation/emission peaks of IRDye800CW in the near-infrared region (780/805 nm) ensure increased penetration depth due to reduced scattering, and higher signal-to-background ratio due to the low autofluorescence of practically all tissues in this spectral region [27].

In this paper, we present *in situ* near-infrared immuno-fluorescence (immuno-NIRF) combined with Optical Coherence Tomography (OCT) using a mouse model bearing human colon cancer. We also present a galvo-based scanner for tumor *ex vivo* examination and an endoscope designed to reach the human lung periphery *in vivo*. With its ~15 µm resolution, immuno-NIRF has the potential to provide microscopic molecular contrast of the TME. OCT provides three-dimensional structure at ~15 µm spatial resolution without additional exogenous contrast agents [29]. Immuno-NIRF and OCT complement each other by visualizing molecular contrast within the surrounding tissue architectural context, in analogy to PET-CT or PET-MRI. The mAb labetuzumab, labeled with a near-infrared fluorescent molecule and the PET isotope zirconium-89, provides molecular whole body and local imaging by targeting the carcinoembryonic antigen (CEA), which is abundantly expressed by colorectal cancer cells. The compound was administered intravenously in live mice three days before imaging, for optimal targeting of the cancer cells. We used the near-infrared cyanine fluorophore IRDye800CW because of its low toxicity, good brightness, and, most importantly, the possibility to conjugate it inertly to antibodies [30]. Recently, IRDye800CW has been the object of several clinical trials focused on intraoperative imaging [31–36], showing its potential for clinical applications.

Biomedical Optics EXPRESS

2. Materials and methods

We developed and assembled a custom-built optical setup and endoscopic scanner designed for *in vivo* imaging in clinical and preclinical settings. In a virtually all-fiber implementation the system efficiently combined and separated OCT and NIRF signals using a double-clad fiber coupler (Fig. 1). Similar designs have shown the combination of OCT with fluorescence imaging [14–21], laser tissue coagulation [37], near-infrared spectroscopy [38], and hyperspectral imaging [39]. The design is versatile in the sense that it can be adapted to detect spectrally separated fluorophores simultaneously, retrieve the tissue autofluorescence, or implement other techniques such as white light spectroscopy.

2.1. Optical setup

Two scanning interfaces were developed, a galvo-based "handheld" scanner and an endoscope designed for imaging lung airways. The use of optical fibers ensures stable optical alignment and easy switching between the handheld scanner and the endoscope. The OCT setup is based on a swept source laser (Axsun Inc., Billerica MA, USA) centered at 1310 nm with a 90 nm bandwidth and 50 kHz sweep rate. A single wavelength of the sweep reflected from a fiber Bragg grating (FBG) functions as a main trigger for the whole system, synchronizing the OCT and NIRF data acquisition to the scanners. A 90/10 beam splitter directs the light into two arms of a Mach-Zehnder interferometer which features a circulator in the sample arm for increased sensitivity, and a spectrally-flat polarization diversity detection unit (PDDM1310, Finisar Corp., Sunnyvale, CA, USA) for optimal balanced detection. The signals from the balanced detectors (PDB430AC, Thorlabs Inc., Newton, NJ, USA) are digitized by a high-speed acquisition card (ATS9350, Alazar Tech. Inc., Pointe-Claire, Canada). The OCT system is combined with the excitation source for fluorescence via an SMF-28 fiber-based wavelength division multiplexer (WD6513A, Thorlabs Inc., Newton, NJ, USA), to maximize 1310 nm throughput, at the cost of slight multimodal operation at the NIRF excitation wavelength. In the NIRF system, light from a single mode diode laser (780CW Thorlabs Inc., NJ, USA) passes through a cleanup filter (FF01-769/41-25, Semrock Inc. Rochester, NY, USA) before being combined with the OCT light. The two signals are incorporated into the single mode core of a double clad coupler (DC1300LEFA Castor Optics, Thorlabs Inc., Newton, NJ, USA). Single-mode illumination is necessary for OCT, and it simultaneously provides a focused excitation beam for better imaging resolution of the fluorescence. The light is delivered to the sample via one of the two scanning devices, either the DCF based endoscope or the 'handheld' scanner. The light scattered back from the sample is collected by both the single mode core and the inner cladding of the DCF fiber. Being an interferometric technique, OCT requires single spatial mode detection and the DCF coupler ensures that the single-mode core light is not mixed with the cladding light and efficiently transmitted (insertion loss <0.5 dB) between the input and output ports. On the other hand, NIRF is an incoherent technique, therefore it benefits from increased collection efficiency by the large 105 μm diameter and 0.2 NA of the first cladding. The DCF coupler extracts about 65% of the cladding light through the 200 μm multimode fiber port. After removing undesired radiation (BLP830RE, cut-on wavelength 832.5 nm, Semrock Inc. Rochester, NY, USA and FESH0900, cut-off wavelength 895.5 nm, Thorlabs Inc., Newton, NJ, USA) the light is coupled into another 200 μm multimode fiber with a light-tight jacket to reduce collection of the ambient light, finally reaching a single-photon avalanche photodetector (SPAD) set in photon counting mode. The SPAD (SPCM-NIR, Excelitas Technologies GmbH, Wiesbaden, Germany) has a dark count rate of 250 count-per-second and a maximum count-rate of 40×10^6 cps, with a detection efficiency of 68% at 800 nm. The output of the SPAD is a series of TTL pulses that are recorded by an acquisition module (PCIe 6259, National Instruments, Austin, TX, USA) and shown in real time together with the OCT B-scans (cross-sections).

Biomedical Optics EXPRESS

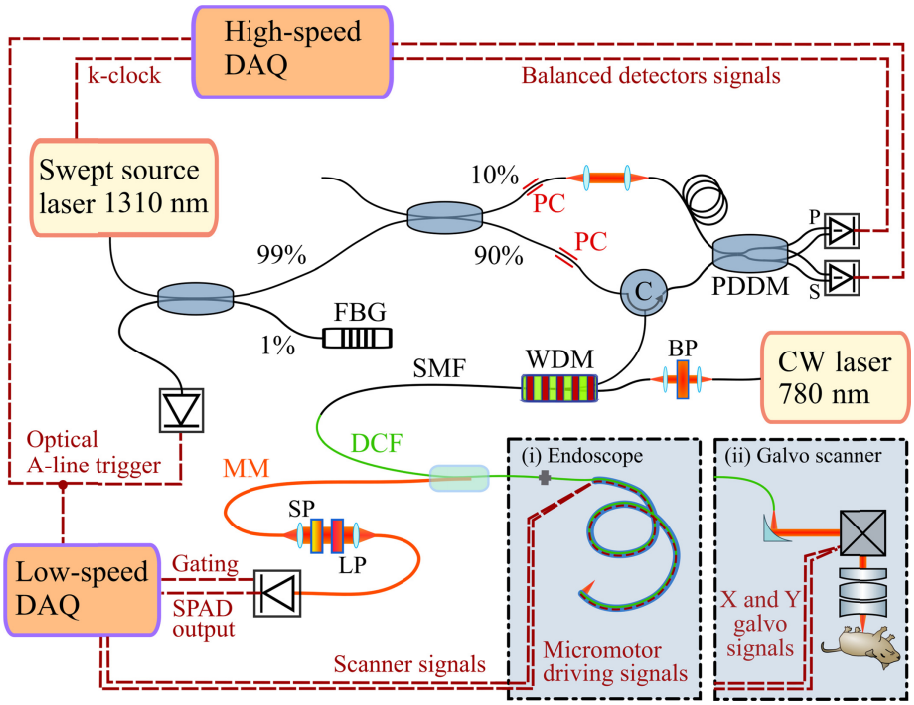

Fig. 1. The optical system combines a single-mode fiber-based swept-source 1310 nm OCT setup with an all-fiber fluorescence system based on continuous wave (CW) excitation at 780 nm. The OCT system is based on a modified Mach-Zehnder interferometer that features a circulator (C) in the sample arm for increased sensitivity and a polarization diversity detection module (PDDM) that splits the interference signals into S and P polarizations before balanced detection. FBG: Fiber Bragg Grating, PC: Polarization Controller, DAQ: Data Acquisition Card. An SMF-28 based wavelength division multiplexer (WDM) combines the OCT light with the fluorescence excitation light of a bandpass filtered (BP) CW laser (780 nm). A double-clad fiber (DCF) coupler delivers the light to the sample, and ensures that the backscattered OCT light travels back to the interferometer through its single-mode core. Conversely, the collected cladding light is extracted into a multimode fiber (MM), filtered by a short-pass filter (SP) and a long-pass filter (LP) to select the emission band of the fluorophore, and finally detected by a single photon avalanche photodiode (SPAD). The DCF coupler can be connected to either an endoscope (i) for imaging internal organs or a galvo-based scanner (ii) to image ex vivo samples or externally accessible organs. The imaging endoscope features a micromotor at the tip to scan the beam circumferentially. The galvo-based "handheld" scanner is composed of a reflective collimator to minimize focal shifts between the different wavelengths, an X-Y galvo scanner pair, and an objective to deliver the light to and collect the light from the sample.

2.2. OCT-NIRF endoscope design

We developed the DCF-based endoscope in-house, building on the design of a motorized single-mode fiber OCT endoscope described earlier [40,41] (Fig. 2). We glued a DCF pigtail (SM-9/105/125-20A Nufern Inc., East Granby CT, USA) to a GRIN lens (GRINTECH GmbH, Jena, Germany), angle-polished to minimize back reflections. A 300 µm prism (Edmund Optics Inc., Barrington, NJ, USA) with an aluminium reflection layer was glued to the axle of a 1-mm diameter micro motor assembled in-house. The angle of incidence of the beam on the pebax endoscope sheath (Arkema, Colombes Cedex, France) throughout the rotation was designed to be always larger than 98° to minimize back reflections detrimental to OCT imaging. The AC motor was actuated with two pi/2 shifted sinusoidal waves at 52 Hz, provided by a custom built endoscope driver synchronized to the rest of the system through the optical trigger of the OCT system.

Biomedical Optics EXPRESS

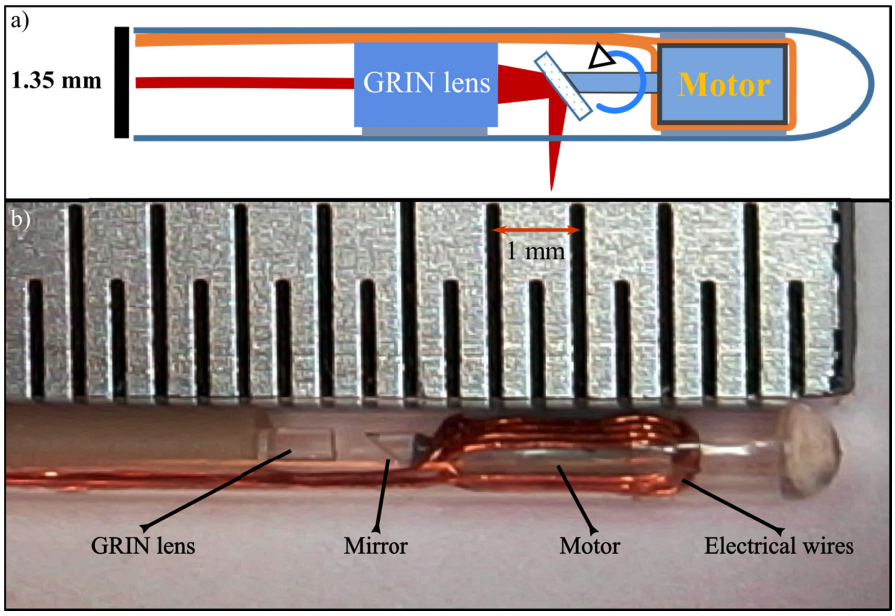

Fig. 2. a) Schematic representation of the DCF-based endoscope. A GRIN lens focuses the light that is transmitted by the single-mode core and scanned circularly by a motorized micromirror. The backscattered light is collected by both the single-mode core and the inner cladding of the DCF. b) photo of the tip of the endoscope. Distance between markers on the ruler is 0.5 mm.

2.3. OCT-NIRF galvo-based scanner

We developed a compact scanner that includes three main elements: a reflective collimator (RC04APC-P01, Thorlabs Inc. Newton NJ, USA), a set of dual-axis galvo scanning mirrors (GVS002, Thorlabs Inc. Newton NJ, USA), and a broadband telecentric optical objective (LSM03BB, Thorlabs Inc. Newton NJ, USA). The benefit of using a reflective collimator over a lens is the reduction of the focal shift between NIRF (800nm) and OCT (1300 nm) excitation, to the measured value of ~40 µm. The optical objective was chosen with an antireflection coating optimized for the 800 nm region because the C-coating (optimized for the 1300 nm region) strongly absorbs the 780 nm radiation. This choice comes at the cost of a noticeable absorption of the 1310 nm OCT radiation, with a transmission loss of about 1 dB.

2.4. Characterization of photoluminescence in DCF silica fibers

The excitation light traveling through the single-mode core of the DCF generates photoluminescence that radiates isotropically, allowing the large-NA cladding of the fiber to collect part of it and guide it back to the SPAD detector. The photoluminescence spectrum was measured by placing the facet of the multimode fiber of the DCF coupler in the focal plane of a Raman microscope with the same NA (Renishaw plc, Wotton-under-Edge, UK), while exciting the fiber core with 1 mW of 780 nm light. The necessity of proper optical filtering of the background was already pointed out by Wang *et al.* [42]. After characterization of the photoluminescence spectrum, we used a longpass filter with a cut-on wavelength of 832.5 nm, which reduced the NIRF signal but improved the signal-to-noise ratio (SNR) because of the diminished background. The magnitude of this radiation increases with the length of fiber involved. We measured this relationship by illuminating the fiber core with constant power and sequentially removing 10 cm long segments of DCF. Because of the DCF coupler design, only the photoluminescence created by the segment of DCF from the coupling region to the output port of the coupler is collected by the MM fiber.

Biomedical Optics EXPRESS

2.5. Characterization of NIRF detection limit and SNR

To demonstrate that avoiding the photoluminescence emitted by the silica fibers is crucial for improving the signal-to-noise ratio, we measured solutions of IRDye800CW of increasing concentration with two different filter settings. Based on the emission spectrum of IRDye800CW (see Fig. 3(a), a long pass filter with cut-on wavelength at 805 nm (BLP785R, Semrock Inc. Rochester, NY, USA) integrates most of the IRDye800CW emission, while collecting also a significant amount of photoluminescence. In comparison, a long pass filter with a cut-on wavelength of 832.5 nm (BLP830RE, Semrock Inc. Rochester, NY, USA) integrates about one sixth of the emitted fluorescence, but allows significantly less photoluminescence to be detected. In both cases, a shortpass filter with 895.5 nm cut-off wavelength was used to effectively reject the OCT light. We compared these filter settings by imaging serum solutions of IRDye800CW to closely mimic the spectral characteristic of the dye in a real situation. For the galvo-based scanner, we placed the focal spot of the objective about 0.5 mm below the surface of the solution, and scanned the mirrors over an area of 1x1 mm^2. We varied the concentration between 0.3 nM and 30 nM, with an excitation power of 575 ± 5 µW. The endoscope was inserted in a sealed glass capillary (1.5 mm internal diameter (ID), 1.9 mm outer diameter (OD)) to avoid contamination of the endoscope and the motor was actuated at the imaging scan rate of 52 rotations/sec. The concentration range was 10 nM to 1 µM, with an excitation power of 175 µW for the narrow band filter combination (832.5 – 895.5nm), and 62 µW for the broadband filter combination (805 - 895.5nm). The excitation power for the broadband filter was reduced to avoid saturation of the detector. For both scanners, 100,000 consecutive measurements with an individual integration time of 20 µs were taken. The SNR in dB was defined as

$$SNR = 10 \cdot \log_{10}\left(\frac{S-B}{\sigma_B}\right) \quad (1)$$

where S is the average measured intensity in counts-per-second from the fluorescent solution, B is the average measured intensity of a blank solution at the same power setting and σ_B its standard deviation.

2.6. NIRF imaging resolution

Even though fluorescence is detected by the first cladding of the DCF, the NIRF optical resolution is largely determined by the point-spread-function (PSF) of the beam originating from the single mode core of the DCF. Indeed, only the molecules present in the volume illuminated by the single-mode core will fluoresce. Because of the different geometry of light illumination and collection in the two scanners, the PSF of the NIRF signal was determined with two different phantoms. For the endoscope, the PSF was measured by scanning a sparse suspension of fluorescent beads (Ex/Em wavelength 715/755 nm, diameter 0.1 µm, F8799, Thermo Fischer, Waltham, MA, USA) in a viscous solution (polyethylene glycol-glycerol-water with ratio 50:10:40). A sealed transparent capillary glass (ID 1.5 mm, OD 1.9 mm) was inserted in the suspension to function as a guide for the endoscope, preventing it to come in direct contact with the beads. The motor of the endoscope was actuated at normal speed (52 fps) and the endoscope was pulled back through the capillary at a speed of 0.2 mm/s to guarantee even sampling density in the two dimensions. The PSF of several isolated beads in the NIRF image was measured by fitting a two-dimensional Gaussian distribution, yielding an average PSF of 15 µm. For the galvo-based scanner, the resolution of the NIRF channel was measured by imaging a fluorescent USAF target (#57-855, Edmund Optics Ltd. UK, York, UK). The smallest feature that can be resolved was in element 1 of group 5, corresponding to a full-width-at-half-maximum of 22.3 µm. The PSF of the beam in the focus generated by the objective is specified to be 18 µm, but the core of the DCF does not guarantee single-mode operation for the NIRF excitation wavelength preventing reaching the theoretical PSF.

Biomedical Optics EXPRESS

2.7. Animal model

Three mice (age, 8-10 weeks; body weight, 22-28 gram; Envigo, Horst, The Netherlands) were injected intraperitoneally (i.p.) in the pelvis with human colon cancer cells. The mice were kept in sterile surroundings at 24°C and 60% humidity with standardized light/dark cycle and access to food and water ad libitum.

Cell line: LS174T colon cancer cells (ATCC CL-188) were cultured in Dulbecco's modified Eagle's medium (DMEM Lonza BE12-709F, supplemented with 1% L-glutamine (Lonza BE17-605E) and 10% fetal bovine serum (FBS; Gibco 10270) at 37 °C, 5% CO_2. Two weeks before imaging, the mice were anaesthetized with inhalation anaesthetics (isoflurane 2–2.5% and oxygen 0.45 volume %) after which $1x10^6$ cells in 300 µL culture medium without FBS were i.p. injected. After imaging with PET-CT and with a wide-field fluorescence imager, the mice were sacrificed and tumor tissue was rapidly excised for further imaging. The freshly excised tumors were not fixed.

Animal experiments were performed according to the criteria and guidelines of European Community Council Directive 2010/63/EU for laboratory animal care and the Dutch Law on animal experimentation. The local committee of the Amsterdam University Medical Center approved the animal experimental protocol.

2.8. Tracer synthesis and PET-CT imaging

Labetuzumab is a complementarity-determining region (CDR)-grafted (humanized) CEA-specific (CEACAM5) immunoglobulin G1 subclass monoclonal antibody that was kindly provided by Dr. D.M. Goldenberg, Immunomedics, Inc. (Morris Plains, NJ) [43]. The compound [89Zr]Zr-labetuzumab-IRDye800CW was synthesized as described previously [30], with a radiochemical purity > 95%. Mice were anaesthetized using inhalation anesthetics (isoflurane 2–2.5% and oxygen 0.45 volume %) and injected retro-orbital with 100 µg of compound (dose 1 MBq, injection volume 100 µL). Three days after injection, the mice were placed on the integrated heating bed of a PET-CT (Mediso nanoPET-CT, Budapest, Hungary) while monitoring respiratory function. A computed tomography (CT) scan was performed for 6 min, followed by a PET scan of 60 min. PET data were normalized, and corrected for scatter, randomization, attenuation, decay and dead time. Thereafter, mice were placed in a wide-field NIR fluorescence imager (In-Vivo Xtreme Imager, Bruker, Leiderdorp, The Netherlands) with excitation and emission filters of 760 nm and 830 nm, respectively for NIR fluorescence imaging for 5 sec. After imaging, the mice were sacrificed and all visible tumor lesions were taken out for *ex vivo* wide-field NIR fluorescence imaging.

2.9. Optical imaging of human colorectal tumors in a xenograft mouse model

After imaging the mice in the PET-CT scanner and the wide-field NIR fluorescence imager, they were sacrificed. Thereafter, a small incision in the skin was made to insert the endoscope for imaging. In this mouse xenograft model, the tumor masses spread across the peritoneum and were not growing inside the lumen of a specific organ. While scanning with the endoscope, the NIRF signal served as a reliable and fast guide, exhibiting a good signal-to-background ratio when a tumor was in its proximity. Once a suspicious location was identified, the endoscope was pulled back at a constant speed of 0.2 mm/s with a linear translation stage (A-LSQ150B, Zaber Technologies Inc. Vancouver, BC, Canada) and about one thousand B-scans at a rate of 52 fps (960 A-lines per B-scan) were acquired. The acquired NIRF data were shown in real time in an *en face* (coronal) image of the scanned area, giving immediate feedback. Moreover, OCT B-scans were displayed continuously at video rate. After the acquisition of several volumes, skin and peritoneum were cut open and the galvo scanner head was positioned above the belly. The fast axis galvo mirror was run continuously providing video rate 1D NIRF and OCT B-scans, which are particularly useful to position the focus at an optimal depth in the tissue. Also in this instance, the NIRF signal

Biomedical Optics EXPRESS

was used as a navigation tool, thanks to its high specificity to tumor locations. Once an interesting location was identified, full OCT C-scan (1000 B-scans of 1000 A-lines) and 2D NIRF images (1000x1000 pixels) were acquired simultaneously. A live composition of a NIRF *en face* image was displayed to give immediate feedback on the image quality. Videos of the volumetric scans for both endoscope and galvo scanner are available as supplementary materials. In this report, the images are shown in inverted order with respect to the chronological acquisition order, first the galvo scanner images of an excised tumor, then *in situ* galvo scanner images, finally an endoscopic scan.

2.10. OCT-NIRF data acquisition and image reconstruction

The measurements were performed in a regular room but with the ceiling lights off and blinded windows. First, a background measurement for the NIRF and a reference arm-only measurement for the OCT were taken. The incident power on the sample was measured before every scan. For the endoscope the incident power was 0.67 mW for the 780 nm NIRF excitation and 10 mW for the 1310 nm OCT. For the galvo-based scanner, the incident power of the NIRF excitation band was 1.0 mW and 9 mW for the OCT, due to the sub-optimal antireflection coating of the objective we used. The raw OCT spectra were acquired equally sampled in k-space and Fourier transformed to create A-lines as described previously [44], with the B-scans eventually displayed with a 55 dB dynamic range. We chose to show the images in inverted grayscale because it improves the visualization of lower-SNR details. The fluorescence raw data were converted into counts-per-second and the factory-provided correction curve for the non-linear response of the SPAD was applied. The data were displayed in grayscale *en face* images, with the lower bound of the grayscale being the background and the upper bound 0.8 times the highest count rate of the image, to maximize the dynamic range. Finally, we displayed the cross-sectional OCT B-scans with the co-registered one-dimensional NIRF along the scanning axis to facilitate the identification of the tumor lesions in the OCT images.

2.11. Automatic OCT B-scan segmentation

A novel method based on shortest path search algorithm [45] was developed, using intensity OCT B-scans in rectangular format without advanced denoising procedures. After computing an integral image and blurring it with a 12-by-12 average Gaussian filter, a vertical gradient (g_z) was calculated. Based on the vertical gradient, a cost function was determined as $1-\frac{g_z}{\max(g_z)}$. Our algorithm was initialized automatically by adding two extra nodes with zero cost before the first and after the last A-line of each B-scan, acting as source and sink of the graph. Finally, the shortest path search to find the minimum cost path among its eight neighboring pixels was applied and the air-to-tissue boundary was found. To precisely find the outer surface of the endoscope sheath, two iterations were necessary. In some situations the tumor protruded considerably along the axial dimension with respect to the rest of the tissue, causing the segmentation algorithm to fail. Therefore, each B-scan was divided into subsections representing either tumor or other tissues, using the tissue-to-tumor boundary determined by segmenting the *en face* NIRF image with the Chen-Vese method [46]. Each subsection was segmented separately, and then merged to cover the whole B-scan.

3. Results

3.1. Characterization of photoluminescence in DCF silica fibers

The fluorescence excitation light propagating in a glass fiber generates photoluminescence, increasing the background and reducing the SNR of NIRF. Figure 3(a) shows the photoluminescence generated by 780 nm light propagating through a passive silica DCF (Nufern SM-9/105/125-20A). From the spectrum shape, and the fact that it shifts with the

Biomedical Optics EXPRESS

excitation wavelength (data not shown) we deduce that the main source of fiber photoluminescence in this spectral region is Raman scattering. Its magnitude was comparable to the fluorescence signal collected from the sample and therefore severely affected the SNR. The intensity of the Raman radiation, normalized by the optical power, increased linearly with the length of DCF, as shown in Fig. 3(b). Noticeably, a weighted linear fit of the data (Raman[Mcps/mW] = 0.0114•Length[cm] + 0.488[Mcps/mW]) does not intercept the origin of the axes, meaning that a residual background signal occurred in the DCF coupler. It is noteworthy that the distal scanning design of our endoscope would allow placing a DCF coupler near the tip, therefore dramatically reducing the segment of DCF giving rise to Raman background.

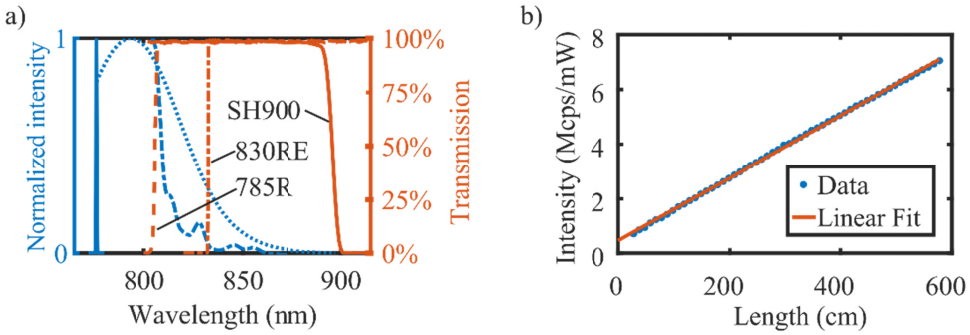

Fig. 3. a) The 780 nm laser excitation linewidth (solid blue), the spectrum of the photoluminescence in silica DCF fiber (dashed-dotted blue), and the emission spectrum of [89Zr]Zr-labetuzumab-IRDye800CW (dotted blue) are shown on a normalized intensity scale. In orange the transmission curves of the optical filters; BLP785R (dashed orange), BLP830RE longpass filter (dashed-dotted orange), and shortpass filter SH900 (solid orange). b) The measured intensity of the photoluminescence for DCF segments of increasing length (blue dots), normalized by the injected optical power, versus a linear-model weighted fitted line (orange solid line). The error bars are not shown because they are too small to be visible.

3.2. Determination of NIRF detection limit and SNR

We assessed the performance of the system by determining its sensitivity. The endoscope exhibited significantly higher Raman background, due to the longer segment of DCF involved: about 250 cm compared to about 30 cm for the handheld scanner.

Figure 4 shows that the narrow band filter ensures an SNR that is 3 dB better than with the broadband filter for the galvo scanner, and 2 dB for the endoscope system. The figure also shows the detection limit for the setup (defined as 3 dB SNR), namely about 0.3 nM for the galvo scanner and about 10 nM for the endoscope.

Biomedical Optics EXPRESS

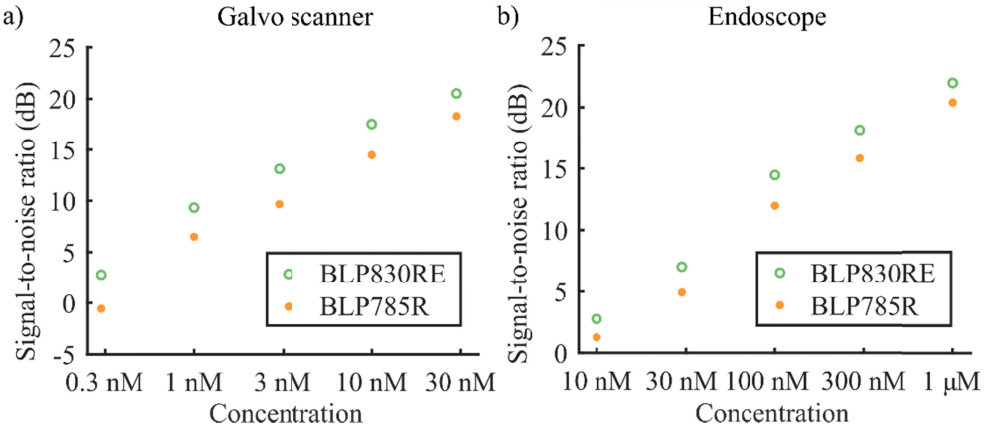

Fig. 4. Log-log plot of the NIRF setup SNR. a) NIRF SNR with the galvo-based scanner in the range 0.3 nM to 30 nM, shown on a logarithmic scale. b) NIRF SNR of the endoscope, in the range 10 nM to 1 µM, shown on a logarithmic scale. The green dots represent the measurements done with filter BLP830RE, while the orange dots the ones done with filter BLP785R. The narrow band filter BLP830RE ensures higher signal-to-noise ratio for both scanners, over the whole range of concentrations.

3.3 Galvo-based scanner imaging

The immuno-NIRF-OCT images are presented in reverse order with respect to the chronological acquisition order, to introduce them in comparison with the state-of-the-art whole-body imaging tools. First *in vivo* PET-CT and wide-field NIR fluorescence images of one of the mice in the study are presented (Fig. 5(a) and Fig. 5(b), respectively). After sacrificing the mouse, the large tumor visible in the center of the peritoneal cavity was excised and imaged with the wide-field NIR fluorescence imager (Fig. 5(c) and successively with our galvo-based probe (Fig. 5(d), from the opposite side because of the opposite geometry of the two scanners. The galvo-based NIRF image is a collage of three adjacent scans. Although simultaneously acquired, OCT images are not shown here to focus on the comparison with wide-field NIRF. Figure 5(e) shows a magnification of the marked red square in Fig. 5(d), which reveals the high level of detail that can be resolved with our imaging system. The white areas (low concentration of mAb) are assumed to be segments of connective tissue (stroma). The radioactivity of the excised tumor was measured with a calibrated gamma counter, yielding a value of about 36.0% injected dose/g. Using the molecular weight of the compound (~$151 \cdot 10^3$ g/mol) and the dose (100 µg) this value can be converted into molar concentration, obtaining an average value of ~240 nM.

Biomedical Optics EXPRESS

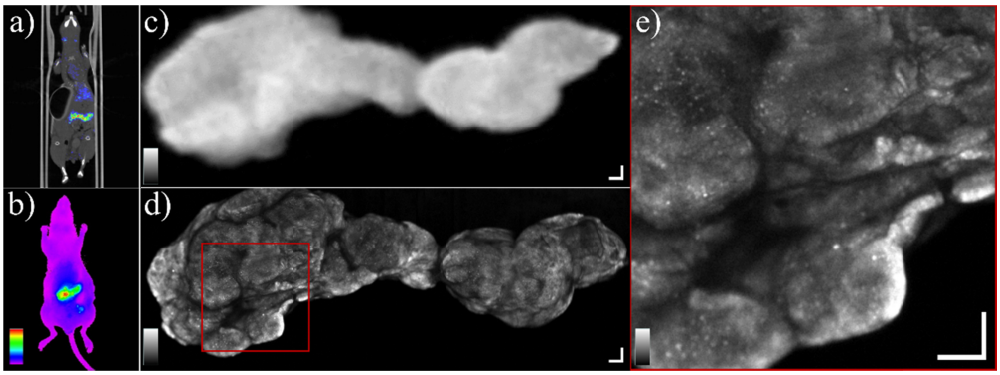

Fig. 5. a) PET-CT image of a mouse bearing LS174T colon cancer xenografts i.p. b) A wide-field NIR fluorescence image of the same mouse showing the accumulation of [89Zr]Zr-labetuzumab-IRDye800CW i.p. The greyscale range is $[5.0–12]\cdot10^6$ photons/s·mm^2. c) The large tumor visible in images (a) and (b) was excised and imaged again *ex vivo* with the wide-field NIR fluorescence imager. The color-scale range is $[4.2–58]\cdot10^6$ photons/s·mm^2. (*i.e.* fluorescence background and maximum value). d) The same excised tumor imaged with our custom NIRF scanner. The tumor was imaged from the opposite side with respect to the wide-field NIR fluorescence imager. The grayscale ranges from the background count rate to 0.8 times the maximum count rate of the image, in numbers: $[1.8–21.6]\cdot10^6$ photons/s. e) Zoomed in view of the area marked by the red square in (d) showing heterogeneity of the tumor. The connective tissue appears as white (low-fluorescence) areas. The greyscale range is $[1.8–21.6]\cdot10^6$ photons/s. All scale bars are 500 µm.

Figure 6 shows NIRF and OCT images acquired *in situ* in the mouse peritoneum, before surgically extracting the tumors. The tumor was found by examining the surface of the exposed belly with the handheld scanner. Figure 6(a) shows the *en face* NIRF image, while Fig. 6(b) shows the corresponding *en face* OCT image, obtained by integrating the OCT C-scan in the depth dimension. The tumor was located next to the liver, which is visible on the left hand side of the images a) and b). The boundaries of the tumor are indicated by the orange contour based on the NIRF image. Four examples of cross-sectional OCT images are shown in images Fig. 6(c-f), which correspond to the locations marked by the black lines in Fig. 6(b). The OCT B-scans show that the tumor protruded significantly from the liver, and that the scattering properties of the two structures are markedly different. For example, Fig. 6(c) shows that the liver structure is very homogenous, with only a blood vessel visible, indicated by the arrow. A video of the sequence of frames is available in supplementary materials.

Biomedical Optics EXPRESS

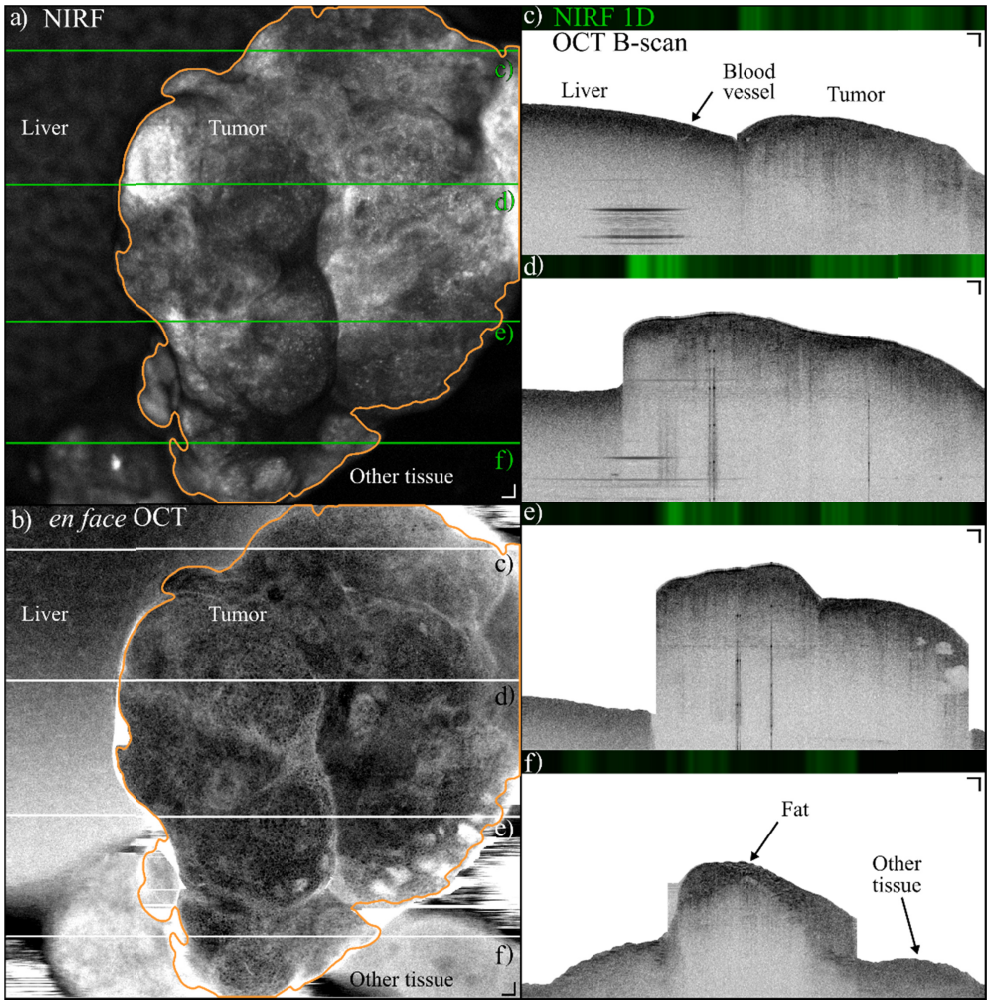

Fig. 6. a) *En face* (coronal) NIRF image of a tumor located next to the liver of the mouse, which is visible on the left side of the image. The tumor is delineated by the orange contour, segmented with a Chen-Vese algorithm, which was used to increase the precision of the OCT segmentation by isolating the tumor portions from the B-scans. The greyscale range is [0.8–9.4]·10^6 photons/s (*i.e.* fluorescence background and 0.8 times the maximum value). b) *En face* OCT projection obtained by integrating OCT intensity over a depth of 880 µm starting from the tissue surface. The liver is visible on the left side of the image. The tumor is delineated by the orange contour obtained from a). c-f) 1-D NIRF and OCT cross sections of the locations marked by the green lines in a) and the black lines in b). The liver structure is remarkably different from the tumor, which shows a higher degree of heterogeneity. Other tissue that was not labeled by the mAb is visible on the right side of image f). The OCT greyscale dynamic range is 55 dB. The tissue surface was segmented from the OCT B-scans with an automated algorithm, which separated areas of tumor from other tissues because the tumor protruded significantly from the rest of the sample. Scale bars are 200 µm. (Visualization 1).

The NIRF and OCT *en face* images shown in Fig. 7(a) and (b), respectively, show another example of a tumor found in the exposed belly of another mouse. The tumor shows a structure of several lobes, which can also be recognized in the OCT *en face* image. A selection of OCT B-scans reveal the structure of the tissue surrounding the tumor, for example fat cells are visible on the right-hand side of Fig. 7(c-d). Because the tumors in this mouse model spread throughout the peritoneum and, for example, do not grow inside the

Biomedical Optics EXPRESS

lumen of an organ, it is difficult to identify the surrounding tissues. A video of the sequence of NIRF and OCT B-scans is available in supplementary materials.

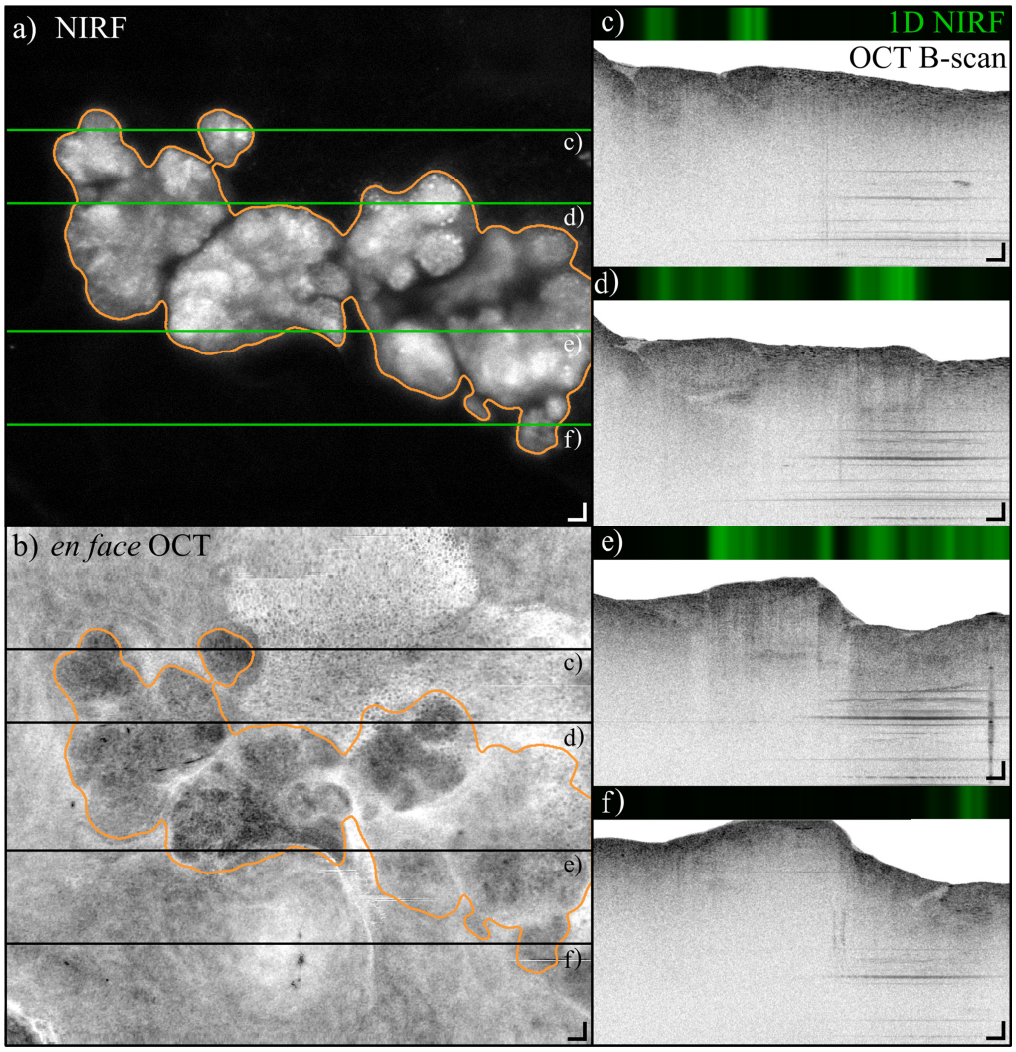

Fig. 7. *In situ* NIRF and OCT images of a tumor located on top of the spleen of one of the mice of the study. a) NIRF image of a tumor mass, showing that tumors developed in several lobes. The tumor is delineated by the orange contour, segmented with a Chen-Vese algorithm. The greyscale range is $[2.2–26.0]\cdot10^6$ photons/s (*i.e.* fluorescence background and 0.8 times the maximum value). b) *en face* (coronal) projection of the OCT scan constructed by integrating the C-scan over a depth of 700 µm starting from the tissue surface. The tumor is delineated by the orange contour obtained from a). c-f) 1-D NIRF and OCT B-scans corresponding to the locations marked with the green lines in a) and black lines in b). The OCT greyscale dynamic range is 55 dB. Scale bars are 100 µm (Visualization 2).

3.4 Endoscopic imaging

Figure 8(a) shows a NIRF scan of a tumor where the vertical dimension corresponds to a full circumferential scan of the motor, while the horizontal dimension is the pullback direction, from left to right.

Figure 8(b) shows the corresponding OCT *en face* representation. A selection of OCT B-Scans with their corresponding NIRF is shown in c-h, taken from several locations along the pullback direction, marked by the green lines in (a) and the black ones in (b). Since the

Biomedical Optics EXPRESS

tumors in this mouse model developed randomly across the peritoneum, *i.e.* not in the lumen of a specific organ, it is difficult to recognize the healthy tissue surrounding the tumor area because it lacks the usual layers found in the lumen of tubular organs.

A video showing the full sequence of frames can be found in the supplementary materials. The outer surface of the endoscope was automatically segmented in each B-scan. The area shadowed by the electrical wires driving the motor was also removed to improve clarity of the image.

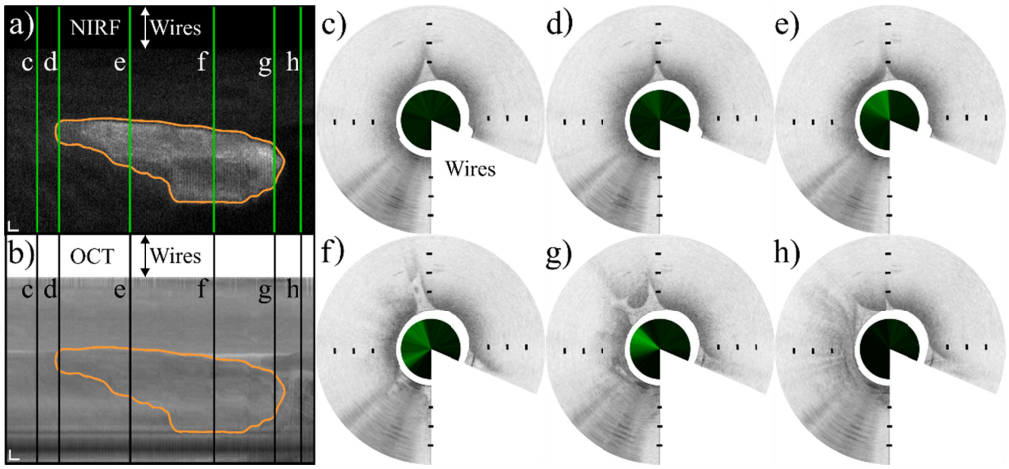

Fig. 8. Combined NIRF and OCT endoscopic images of a tumor located in the peritoneal cavity. a) and b) show NIRF and *en face* OCT images of the tumor, respectively, unwrapped along the circumference of the endoscope. The NIRF greyscale range is $[1.1–3.5]\cdot10^6$ photons/s (*i.e.* fluorescence background and maximum value). The *en face* OCT projection was obtained by integrating OCT intensity over a depth of 500 µm starting from the tissue surface. The vertical axis represents the circumference of the endoscope, the horizontal axis represents the pullback direction over a distance of 5 mm, from left to right. Scale bars 200 µm. The tumor is delineated by the orange contour obtained similarly to Fig. (7) and 8. Figs. (c-h) show cross sectional images taken from sequential locations along the pullback, indicated by the vertical green lines in a) and the black lines in b), from left to right. The inner circles show the one-dimensional NIRF data surrounded by the OCT cross sections segmented starting from the endoscope outer sheath. The white wedge of each B-scan masks the area of tissue blocked by the electrical wires. Distance between markers 0.5 mm (Visualization 3).

4. Discussion

To the best of our knowledge, this is the first demonstration of *in situ* immuno-NIRF imaging of tumors at this scale, in combination with structural imaging. The current tools that are able to image the biodistribution of monoclonal antibodies labeled with IRDye800CW are all based on wide-field fluorescence [31–34,47–49]. Wide-field fluorescence allows video-rate intraoperative imaging, but it does not provide structural information and it is limited in resolution, preventing the sharp delineation of tumor boundaries. Our proposed immuno-NIRF-OCT method can overcome these limitations, providing high resolution molecular imaging and structural information on the surveyed tissue.

The NIRF images revealed a high degree of heterogeneity of the tumor masses in all the mice. This is particularly striking when these images are compared with the PET and the wide-field NIR fluorescence images of the same masses, which do not reveal a similar level of detail. For example, Fig. 5(d) shows tracks of very low accumulation of the mAbs, assumed to be segments of stroma. Figure 5(e) reveals in high detail the tumor heterogeneity. Moreover, there are sparse locations of high accumulation of mAbs that seem smaller than the resolution of our device, suggesting that the signal originates from a small group of cells. Although the perceived heterogeneity could arise from a non-receptor-saturating dose, the cell line used in this xenograft model is known to form highly heterogeneous tumors [50] and

Biomedical Optics EXPRESS

therefore a non-uniform distribution of antibodies is expected, even at high doses. Importantly, NIRF imaging also allows a direct identification of the tumor mass in the OCT cross sections, for example, in Fig. 6(c-e). OCT imaging provides the tissue architectural context that helps in further distinguishing the various tissues, and possibly gives information on the tumor infiltration in the mucosa and submucosa.

We envision the introduction of immuno-NIRF-OCT imaging as an addition to the current nuclear/fluorescence imaging and a firm step to come to "non-invasive in vivo immunohistochemistry", allowing to study tumor responses to newly developed immunotherapeutic antibodies at a scale that is not otherwise accessible. It would also enable longitudinal studies within the same patient since endoscopic immuno-NIRF-OCT has the potential to reduce the necessity of biopsy sampling. This could be very beneficial to unveil the mechanisms at the base of resistance to immunotherapy for particular subgroups of patients. Since immuno-NIRF provides excellent contrast, it could aid in the diagnosis, provided that a suitable mAb target can be found. Moreover, it would be interesting to attach spectrally separated fluorophores to various mAb and/or ligands, opening the possibility to visualize antibody-ligand and cell-cell interactions, not achievable with nuclear imaging. The NIRF-OCT endoscope was designed to be inserted thorough the working channel of commercial bronchoscopes and deployed to the site of interest in the central or peripheral airways, as an addition to the standard procedure. Due to its small size, another possible application of the endoscope is bile duct imaging. Importantly, the detection sensitivity of our setup suggests that antibody concentrations anticipated in a person injected with a micro-dose of immuno-imaging agents can be detected, which is important to facilitate the path towards use in humans. For instance, by quantifying the uptake of immuno-PET tracers in tumors, it is possible to estimate the local concentration of the injected antibody in a tumor, in humans [51]. By injecting a micro-dose of mAbs (about 4.5 mg in an adult human, the molecular weight of a typical fluorescently labeled mAb is $\sim 151 \cdot 10^3$ g/mol), a typical accumulation of 0.020% injected dose/gram can be expected in a tumor, translating to an average mAb-PET tracer concentration of about 6 nM in a tumor, with the sensitivity of our endoscope close to this target while the one of the galvo-based scanner well within. As for more immediate clinical applications, this platform would also allow to delineate the tumor margins with high accuracy and to laser-mark its boundaries. The added value of the structural imaging provided by OCT in this context is multifold. For example, one could assess the stage of progression/regression of the disease by visualizing the degree of penetration of the tumor into the mucosa and submucosa. Importantly, OCT could provide a means to determine the optical properties of the tissue, helping to quantify the absolute intensity of the NIRF signal and in turn, the antibody uptake. Finally, OCT is able to resolve the microvasculature network in three dimensions, without exogenous contrast agents, providing valuable information on the tumor activity [52].

As for technical considerations on the quality of the images, the immuno-NIRF images generated with the galvo scanner are superior to the endoscope ones. One reason is the background noise generated in the fiber is increased for the endoscope, since the length of DCF is about 250 cm for the endoscope, compared to about 30 cm for the galvo-based scanner. Also, the insertion and transmission losses of the NIRF excitation and collection are higher in the endoscope by about a factor of two. The endoscope includes miniaturized optical elements such as the GRIN lens and an aluminum coated microprism, which has a reflectivity of only 75% at 800 nm. From our simulations, it appears that the collection cone of the cladding is slightly overfilling the mirror, giving a sub-optimal collection efficiency throughout the rotation. Finally, the chromatic aberration induced by the GRIN lens causes the NIRF beam to focus about 175 µm more superficially than the OCT, leading to suboptimal excitation fluence deeper in the tissue. The DCF fiber affects the galvo scanner (30 cm DCF) and endoscope (250 cm DCF) OCT images. Coupling of the backscattered OCT light transported through the DCF cladding into the single mode core at the junction between

Biomedical Optics EXPRESS

the DCF coupler and the SMF exhibits different behavior because of the different length of DCF involved. In the galvo scanner case, this cross talk creates a semi-coherent image that appears as an echo above the confocal OCT images, because of the lower refractive index of the cladding. For the endoscope, the cross talk prevents shot-noise-limited detection because of increased radiation reaching the photodetectors, but it does not create an echo because it falls out of the coherence length of the laser.

In conclusion, immuno-NIRF-OCT enables minimally invasive imaging of tumors with high resolution, complementing nuclear imaging by providing high definition molecular and structural images of the TME.

Supplementary materials

Videos sequences of OCT B-scans and NIRF scans corresponding to Figs. 6, 7 and 8 are provided as supplementary materials.

Contributions

All authors contributed to the manuscript. FF designed and built the imaging system, characterized Raman scattering of fibers and produced the NIRF and OCT images. FF, HK, MV, CFMM designed and executed the experiments. HK measured the spectral properties of IRDye800. VD and FF wrote the segmentation algorithm. FF, CFMM, HK, VD, DJV, GAMSvD and JFdB wrote and reviewed the manuscript. JFdB and GAMSvD developed the concept of Immuno-NIRF-OCT and JFdB supervised the project.

Funding

Netherlands Organization for Scientific Research (NWO) with a Vici (JFdB) grant (918.10.628); European Union's Horizon 2020 research and innovation program (654148) LaserLaB Europe (JFdB).

Acknowledgments

We would like to thank the technicians of the VU University workshop; Dick van Iperen for making the endoscope, Han Voet, Wesley Delmeer, and Rob J. Limburg for developing the drivers of the endoscope motor and the galvo scanners, and Joost C. Rosier for coordinating the technical efforts. We thank Bram Mooij for help in the development of the system, Margherita Vaselli for helping with the resolution measurements and Jelmer J. Weda for making the phantoms and technical support. Freek Ariese for discussion over the IRDye800CWspectra. Oleg Nadyarnykh and Ben Lochocki for help during the imaging sessions. David Goldenberg is thanked for providing the antibody labetuzumab. Joey Muns and Iris Mes are greatly acknowledged for labeling of the antibody and Ricardo Vos for help with operating the PET-CT.

Disclosures

The authors declare that they have no conflict of interest.

References

1. D. B. Page, M. A. Postow, M. K. Callahan, J. P. Allison, and J. D. Wolchok, “Immune Modulation in Cancer with Antibodies,” in *Annual Review of Medicine, Vol 65*, C. T. Caskey, ed. (Annual Reviews, Palo Alto, 2014), pp. 185+.
2. S. Goel, D. G. Duda, L. Xu, L. L. Munn, Y. Boucher, D. Fukumura, and R. K. Jain, “Normalization of the vasculature for treatment of cancer and other diseases,” Physiol. Rev. **91**(3), 1071–1121 (2011).
3. R. V. J. Chari, M. L. Miller, and W. C. Widdison, “Antibody-Drug Conjugates: An Emerging Concept in Cancer Therapy,” Angew. Chem. Int. Ed. Engl. **53**(15), 3796–3827 (2014).
4. S. Panowski, S. Bhakta, H. Raab, P. Polakis, and J. R. Junutula, “Site-specific antibody drug conjugates for cancer therapy,” MAbs **6**(1), 34–45 (2014).
5. M. Hölzel, A. Bovier, and T. Tüting, “Plasticity of tumour and immune cells: a source of heterogeneity and a cause for therapy resistance?” Nat. Rev. Cancer **13**(5), 365–376 (2013).

Biomedical Optics EXPRESS

6. A. Pèlegrin, S. Folli, F. Buchegger, J. P. Mach, G. Wagnières, and H. van den Bergh, "Antibody-fluorescein conjugates for photoimmunodiagnosis of human colon carcinoma in nude mice," Cancer **67**(10), 2529–2537 (1991).
7. S. Folli, P. Westermann, D. Braichotte, A. Pèlegrin, G. Wagnières, H. van den Bergh, and J. P. Mach, "Antibody-indocyanin conjugates for immunophotodetection of human squamous cell carcinoma in nude mice," Cancer Res. **54**(10), 2643–2649 (1994).
8. S. Folli, G. Wagnières, A. Pèlegrin, J. M. Calmes, D. Braichotte, F. Buchegger, Y. Chalandon, N. Hardman, C. Heusser, J. C. Givel, G. Chapuis, A. Chatelain, H. Vandenbergh, and J. P. Mach, "Immunophotodiagnosis of colon carcinomas in patients injected with fluoresceinated chimeric antibodies against carcinoembryonic antigen," Proc. Natl. Acad. Sci. U.S.A. **89**(17), 7973–7977 (1992).
9. E. L. Rosenthal, B. D. Kulbersh, R. D. Duncan, W. Zhang, J. S. Magnuson, W. R. Carroll, and K. Zinn, "In vivo detection of head and neck cancer orthotopic xenografts by immunofluorescence," Laryngoscope **116**(9), 1636–1641 (2006).
10. R. Cohen, M. A. Stammes, I. H. C. de Roos, M. Stigter-van Walsum, G. W. M. Visser, and G. A. van Dongen, "Inert coupling of IRDye800CW to monoclonal antibodies for clinical optical imaging of tumor targets," EJNMMI Res. **1**(1), 31 (2011).
11. A. L. Vahrmeijer, M. Hutteman, J. R. van der Vorst, C. J. H. van de Velde, and J. V. Frangioni, "Image-guided cancer surgery using near-infrared fluorescence," Nat. Rev. Clin. Oncol. **10**(9), 507–518 (2013).
12. A. A. Lammertsma, "Forward to the Past: The Case for Quantitative PET Imaging," J. Nucl. Med. **58**(7), 1019–1024 (2017).
13. A. R. Tumlinson, L. P. Hariri, U. Utzinger, and J. K. Barton, "Miniature endoscope for simultaneous optical coherence tomography and laser-induced fluorescence measurement," Appl. Opt. **43**(1), 113–121 (2004).
14. S. Y. Ryu, H. Y. Choi, J. Na, E. S. Choi, and B. H. Lee, "Combined system of optical coherence tomography and fluorescence spectroscopy based on double-cladding fiber," Opt. Lett. **33**(20), 2347–2349 (2008).
15. S. Yuan, C. A. Roney, J. Wierwille, C. W. Chen, B. Xu, G. Griffiths, J. Jiang, H. Ma, A. Cable, R. M. Summers, and Y. Chen, "Co-registered optical coherence tomography and fluorescence molecular imaging for simultaneous morphological and molecular imaging," Phys. Med. Biol. **55**(1), 191–206 (2010).
16. H. Yoo, J. W. Kim, M. Shishkov, E. Namati, T. Morse, R. Shubochkin, J. R. McCarthy, V. Ntziachristos, B. E. Bouma, F. A. Jaffer, and G. J. Tearney, "Intra-arterial catheter for simultaneous microstructural and molecular imaging in vivo," Nat. Med. **17**(12), 1680–1684 (2011).
17. J. Xi, Y. Chen, Y. Zhang, K. Murari, M.-J. Li, and X. Li, "Integrated multimodal endomicroscopy platform for simultaneous en face optical coherence and two-photon fluorescence imaging," Opt. Lett. **37**(3), 362–364 (2012).
18. J. Mavadia, J. Xi, Y. Chen, and X. Li, "An all-fiber-optic endoscopy platform for simultaneous OCT and fluorescence imaging," Biomed. Opt. Express **3**(11), 2851–2859 (2012).
19. D. Lorenser, B. C. Quirk, M. Auger, W. J. Madore, R. W. Kirk, N. Godbout, D. D. Sampson, C. Boudoux, and R. A. McLaughlin, "Dual-modality needle probe for combined fluorescence imaging and three-dimensional optical coherence tomography," Opt. Lett. **38**(3), 266–268 (2013).
20. H. Pahlevaninezhad, A. M. D. Lee, T. Shaipanich, R. Raizada, L. Cahill, G. Hohert, V. X. D. Yang, S. Lam, C. MacAulay, and P. Lane, "A high-efficiency fiber-based imaging system for co-registered autofluorescence and optical coherence tomography," Biomed. Opt. Express **5**(9), 2978–2987 (2014).
21. S. Lee, M. W. Lee, H. S. Cho, J. W. Song, H. S. Nam, D. J. Oh, K. Park, W. Y. Oh, H. Yoo, and J. W. Kim, "Fully integrated high-speed intravascular optical coherence tomography/near-infrared fluorescence structural/molecular imaging in vivo using a clinically available near-infrared fluorescence-emitting indocyanine green to detect inflamed lipid-rich atheromata in coronary-sized vessels," Circ. Cardiovasc. Interv. **7**(4), 560–569 (2014).
22. B. E. Sherlock, J. E. Phipps, J. Bec, and L. Marcu, "Simultaneous, label-free, multispectral fluorescence lifetime imaging and optical coherence tomography using a double-clad fiber," Opt. Lett. **42**(19), 3753–3756 (2017).
23. S. Y. Ryu, H. Y. Choi, M. J. Ju, J. Na, W. J. Choi, and B. H. Lee, "The development of double clad fiber and double clad fiber coupler for fiber based biomedical imaging systems," J. Opt. Soc. Korea **13**(3), 310–315 (2009).
24. W. J. Madore, E. De Montigny, O. Ouellette, S. Lemire-Renaud, M. Leduc, X. Daxhelet, N. Godbout, and C. Boudoux, "Asymmetric double-clad fiber couplers for endoscopy," Opt. Lett. **38**(21), 4514–4517 (2013).
25. S. Liang, A. Saidi, J. Jing, G. Liu, J. Li, J. Zhang, C. Sun, J. Narula, and Z. Chen, "Intravascular atherosclerotic imaging with combined fluorescence and optical coherence tomography probe based on a double-clad fiber combiner," J. Biomed. Opt. **17**(7), 070501 (2012).
26. L. Scolaro, D. Lorenser, W. J. Madore, R. W. Kirk, A. S. Kramer, G. C. Yeoh, N. Godbout, D. D. Sampson, C. Boudoux, and R. A. McLaughlin, "Molecular imaging needles: dual-modality optical coherence tomography and fluorescence imaging of labeled antibodies deep in tissue," Biomed. Opt. Express **6**(5), 1767–1781 (2015).
27. J. V. Frangioni, "In vivo near-infrared fluorescence imaging," Curr. Opin. Chem. Biol. **7**(5), 626–634 (2003).
28. M. Gao, F. Yu, C. Lv, J. Choo, and L. Chen, "Fluorescent chemical probes for accurate tumor diagnosis and targeting therapy," Chem. Soc. Rev. **46**(8), 2237–2271 (2017).
29. D. Huang, E. A. Swanson, C. P. Lin, J. S. Schuman, W. G. Stinson, W. Chang, M. R. Hee, T. Flotte, K. Gregory, C. A. Puliafito, and J. G. Fujimoto, "Optical coherence tomography," Science **254**(5035), 1178–1181 (1991).

Biomedical Optics EXPRESS

30. R. Cohen, D. J. Vugts, M. Stigter-van Walsum, G. W. M. Visser, and G. A. M. S. van Dongen, "Inert coupling of IRDye800CW and zirconium-89 to monoclonal antibodies for single- or dual-mode fluorescence and PET imaging," Nat. Protoc. **8**(5), 1010–1018 (2013).
31. E. de Boer, N. J. Harlaar, A. Taruttis, W. B. Nagengast, E. L. Rosenthal, V. Ntziachristos, and G. M. van Dam, "Optical innovations in surgery," Br. J. Surg. **102**(2), e56–e72 (2015).
32. E. L. Rosenthal, J. M. Warram, E. de Boer, T. K. Chung, M. L. Korb, M. Brandwein-Gensler, T. V. Strong, C. E. Schmalbach, A. B. Morlandt, G. Agarwal, Y. E. Hartman, W. R. Carroll, J. S. Richman, L. K. Clemons, L. M. Nabell, and K. R. Zinn, "Safety and Tumor Specificity of Cetuximab-IRDye800 for Surgical Navigation in Head and Neck Cancer," Clin. Cancer Res. **21**(16), 3658–3666 (2015).
33. J. J. Tjalma, P. B. Garcia-Allende, E. Hartmans, A. G. Terwisscha van Scheltinga, W. Boersma-van Ek, J. Glatz, M. Koch, Y. J. van Herwaarden, T. M. Bisseling, I. D. Nagtegaal, H. Timmer-Bosscha, J. J. Koornstra, A. Karrenbeld, J. H. Kleibeuker, G. M. van Dam, V. Ntziachristos, and W. B. Nagengast, "Molecular Fluorescence Endoscopy Targeting Vascular Endothelial Growth Factor A for Improved Colorectal Polyp Detection," J. Nucl. Med. **57**(3), 480–485 (2016).
34. R. R. Zhang, A. B. Schroeder, J. J. Grudzinski, E. L. Rosenthal, J. M. Warram, A. N. Pinchuk, K. W. Eliceiri, J. S. Kuo, and J. P. Weichert, "Beyond the margins: real-time detection of cancer using targeted fluorophores," Nat. Rev. Clin. Oncol. **14**(6), 347–364 (2017).
35. M. C. Boonstra, B. Tolner, B. E. Schaafsma, L. S. F. Boogerd, H. A. J. M. Prevoo, G. Bhavsar, P. J. K. Kuppen, C. F. M. Sier, B. A. Bonsing, J. V. Frangioni, C. J. H. van de Velde, K. A. Chester, and A. L. Vahrmeijer, "Preclinical evaluation of a novel CEA-targeting near-infrared fluorescent tracer delineating colorectal and pancreatic tumors," Int. J. Cancer **137**(8), 1910–1920 (2015).
36. L. S. F. Boogerd, C. E. S. Hoogstins, D. P. Schaap, M. Kusters, H. J. M. Handgraaf, M. J. M. van der Valk, D. E. Hilling, F. A. Holman, K. C. M. J. Peeters, J. S. D. Mieog, C. J. H. van de Velde, A. Farina-Sarasqueta, I. van Lijnschoten, B. Framery, A. Pèlegrin, M. Gutowski, S. W. Nienhuijs, I. H. J. T. de Hingh, G. A. P. Nieuwenhuijzen, H. J. T. Rutten, F. Cailler, J. Burggraaf, and A. L. Vahrmeijer, "Safety and effectiveness of SGM-101, a fluorescent antibody targeting carcinoembryonic antigen, for intraoperative detection of colorectal cancer: a dose-escalation pilot study," Lancet Gastroenterol. Hepatol. **3**(3), 181–191 (2018).
37. K. Beaudette, H. W. Baac, W. J. Madore, M. Villiger, N. Godbout, B. E. Bouma, and C. Boudoux, "Laser tissue coagulation and concurrent optical coherence tomography through a double-clad fiber coupler," Biomed. Opt. Express **6**(4), 1293–1303 (2015).
38. A. M. Fard, P. Vacas-Jacques, E. Hamidi, H. Wang, R. W. Carruth, J. A. Gardecki, and G. J. Tearney, "Optical coherence tomography--near infrared spectroscopy system and catheter for intravascular imaging," Opt. Express **21**(25), 30849–30858 (2013).
39. R. Guay-Lord, X. Attendu, K. L. Lurie, L. Majeau, N. Godbout, A. K. E. Bowden, M. Strupler, and C. Boudoux, "Combined optical coherence tomography and hyperspectral imaging using a double-clad fiber coupler," J. Biomed. Opt. **21**(11), 116008 (2016).
40. J. Li, M. de Groot, F. Helderman, J. Mo, J. M. A. Daniels, K. Grünberg, T. G. Sutedja, and J. F. de Boer, "High speed miniature motorized endoscopic probe for optical frequency domain imaging," Opt. Express **20**(22), 24132–24138 (2012).
41. J. Li, F. Feroldi, J. de Lange, J. M. A. Daniels, K. Grünberg, and J. F. de Boer, "Polarization sensitive optical frequency domain imaging system for endobronchial imaging," Opt. Express **23**(3), 3390–3402 (2015).
42. H. Wang, J. A. Gardecki, G. J. Ughi, P. V. Jacques, E. Hamidi, and G. J. Tearney, "Ex vivo catheter-based imaging of coronary atherosclerosis using multimodality OCT and NIRAF excited at 633 nm," Biomed. Opt. Express **6**(4), 1363–1375 (2015).
43. H. J. Hansen, D. M. Goldenberg, E. S. Newman, R. Grebenau, and R. M. Sharkey, "Characterization of second-generation monoclonal antibodies against carcinoembryonic antigen," Cancer **71**(11), 3478–3485 (1993).
44. B. Braaf, K. A. Vermeer, V. A. Sicam, E. van Zeeburg, J. C. van Meurs, and J. F. de Boer, "Phase-stabilized optical frequency domain imaging at 1-μm for the measurement of blood flow in the human choroid," Opt. Express **19**(21), 20886–20903 (2011).
45. E. W. Dijkstra, "A note on two problems in connexion with graphs," Numer. Math. **1**(1), 269–271 (1959).
46. T. F. Chan and L. A. Vese, "Active contours without edges," IEEE Trans. Image Process. **10**(2), 266–277 (2001).
47. G. M. van Dam, G. Themelis, L. M. A. Crane, N. J. Harlaar, R. G. Pleijhuis, W. Kelder, A. Sarantopoulos, J. S. de Jong, H. J. G. Arts, A. G. J. van der Zee, J. Bart, P. S. Low, and V. Ntziachristos, "Intraoperative tumor-specific fluorescence imaging in ovarian cancer by folate receptor-α targeting: first in-human results," Nat. Med. **17**(10), 1315–1319 (2011).
48. N. J. Harlaar, M. Koller, S. J. de Jongh, B. L. van Leeuwen, P. H. Hemmer, S. Kruijff, R. J. van Ginkel, L. B. Been, J. S. de Jong, G. Kats-Ugurlu, M. D. Linssen, A. Jorritsma-Smit, M. van Oosten, W. B. Nagengast, V. Ntziachristos, and G. M. van Dam, "Molecular fluorescence-guided surgery of peritoneal carcinomatosis of colorectal origin: a single-centre feasibility study," Lancet Gastroenterol. Hepatol. **1**(4), 283–290 (2016).
49. M. Koch, J. S. de Jong, J. Glatz, P. Symvoulidis, L. E. Lamberts, A. L. L. Adams, M. E. G. Kranendonk, A. G. T. Terwisscha van Scheltinga, M. Aichler, L. Jansen, J. de Vries, M. N. Lub-de Hooge, C. P. Schröder, A. Jorritsma-Smit, M. D. Linssen, E. de Boer, B. van der Vegt, W. B. Nagengast, S. G. Elias, S. Oliveira, A. J. Witkamp, W. P. T. M. Mali, E. Van der Wall, P. B. Garcia-Allende, P. J. van Diest, E. G. E. de Vries, A. Walch,

Biomedical Optics EXPRESS

G. M. van Dam, and V. Ntziachristos, "Threshold Analysis and Biodistribution of Fluorescently Labeled Bevacizumab in Human Breast Cancer," Cancer Res. **77**(3), 623–631 (2017).
50. E. El Emir, U. Qureshi, J. L. J. Dearling, G. M. Boxer, I. Clatworthy, A. A. Folarin, M. P. Robson, S. Nagl, M. A. Konerding, and R. B. Pedley, "Predicting Response to Radioimmunotherapy from the Tumor Microenvironment of Colorectal Carcinomas," Cancer Res. **67**(24), 11896–11905 (2007).
51. G. A. Van Dongen, M. C. Huisman, R. Boellaard, N. Harry Hendrikse, A. D. Windhorst, G. W. M. Visser, C. F. M. Molthoff, and D. J. Vugts, "89Zr-immuno-PET for imaging of long circulating drugs and disease targets: why, how and when to be applied?" Q. J. Nucl. Med. Mol. Imaging **59**(1), 18–38 (2015).
52. B. J. Vakoc, D. Fukumura, R. K. Jain, and B. E. Bouma, "Cancer imaging by optical coherence tomography: preclinical progress and clinical potential," Nat. Rev. Cancer **12**(5), 363–368 (2012).